Engineering Cellular Response Using Nanopatterned Bulk Metallic Glass

Jagannath Padmanabhan,[†,‡] Emily R. Kinser,[†,§,⊥] Mark A. Stalter,[⊥] Christopher Duncan-Lewis,[†] Jenna L. Balestrini,[†,∥] Andrew J. Sawyer,[∥] Jan Schroers,[†,§] and Themis R. Kyriakides[†,‡,∥,*]

[†]Center for Research on Interface Structures and Phenomena, Yale University, New Haven, Connecticut 06520, United States, [‡]Department of Biomedical Engineering, Yale University, New Haven, Connecticut 06520, United States, [§]Department of Mechanical Engineering and Materials Science, Yale University, New Haven, Connecticut 06520, United States, [⊥]IBM Semiconductor Research and Development Center, Hopewell Junction, New York 12533, United States, and [∥]Department of Pathology, Yale University, New Haven, Connecticut 06520, United States

ABSTRACT Nanopatterning of biomaterials is rapidly emerging as a tool to engineer cell function. Bulk metallic glasses (BMGs), a class of biocompatible materials, are uniquely suited to study nanopattern–cell interactions as they allow for versatile fabrication of nanopatterns through thermoplastic forming. Work presented here employs nanopatterned BMG substrates to explore detection of nanopattern feature sizes by various cell types, including cells that are associated with foreign body response, pathology, and tissue repair. Fibroblasts decreased in cell area as the nanopattern feature size increased, and fibroblasts could detect nanopatterns as small as 55 nm in size. Macrophages failed to detect nanopatterns of 150 nm or smaller in size, but responded to a feature size of 200 nm, resulting in larger and more elongated cell morphology. Endothelial cells responded to nanopatterns of 100 nm or larger in size by a significant decrease in cell size and elongation. On the basis of these observations, nondimensional analysis was employed to correlate cellular morphology and substrate nanotopography. Analysis of the molecular pathways that induce cytoskeletal remodeling, in conjunction with quantifying cell traction forces with nanoscale precision using a unique FIB-SEM technique, enabled the characterization of underlying biomechanical cues. Nanopatterns altered serum protein adsorption and effective substrate stiffness, leading to changes in focal adhesion density and compromised activation of Rho-A GTPase in fibroblasts. As a consequence, cells displayed restricted cell spreading and decreased collagen production. These observations suggest that topography on the nanoscale can be designed to engineer cellular responses to biomaterials.

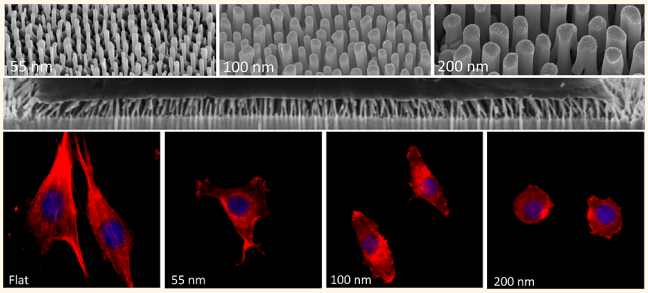

KEYWORDS: bulk metallic glass · biomaterials · nanorods · cell–nanopattern interactions · mechanosensing · traction force measurement

Novel patterning technologies have expanded the fundamental understanding of cellular function at the nano level, a new length scale in cell biology. Nanopatterning can be incorporated into implant design to increase the function and longevity of biomaterials and devices by orchestrating cellular responses, including the foreign body response (FBR). Moreover, nanopatterned biomaterials provide a unique platform to assess cellular responses to topographical cues.

Although nanoscale topography has been exploited with polymers, ceramics, and metals to investigate cellular response, limitations exist with these major material classes. Surface engineering of materials for biomedical applications demands consideration of multiple factors, including manufacturability, targeted *in vivo* functionality, and biocompatibility. Presently, engineered materials have limitations to meet all of these requirements. For example, nanopatterned polymers represent a readily manufacturable and cost-effective tool that can provide fundamental understanding of nanopattern–cell interactions; however, the comparably low yield strength and elastic modulus limit the range of applicability as structural biomaterials.[1−4] In contrast, silicon allows formation of intricate small-scale, high aspect ratio nanopatterned structures,[5,6] but

* Address correspondence to themis.kyriakides@yale.edu.

Received for review November 27, 2013 and accepted April 11, 2014.

Published online April 11, 2014
10.1021/nn501874q

undesirable mechanical properties and lack of biocompatibility limit its use in biomedical applications. Metals and metallic alloys such as titanium and stainless steel alloys have a high strength and stiffness and can be used to provide structural support or replace hard tissues, yet intrinsic length scale restrictions imposed by the grain size of conventional metals pose a challenge to achieve nanoscale feature sizes.[7,8] A continuing need exists for biomaterials having strength and stiffness comparable to metals with the processability akin to polymers.

Versatile chemistry and amorphous atomic structure of BMGs enable a range of compositions that combine processability, as quantified by glass forming ability, and biocompatibility.[9,10] In addition, the mechanical properties of BMGs combine elasticity, strength, and ductility, particularly when used at the nanoscale.[11−14] Moreover, the unique processability of BMGs enables thermoplastic forming (TPF) in a nonrestrictive environment to produce a broad range of novel nanopatterned structures.[15]

Work presented here employs nanopatterned BMG substrates produced using TPF to explore detection of nanopattern feature sizes by various cell types. BMG nanorod arrays with feature sizes ranging from 55 to 200 nm were produced. Three cell types, namely, fibroblasts, macrophages, and endothelial cells were analyzed for nanopattern-induced cytoskeletal remodeling. Fibroblasts, which mediate fibrosis and encapsulation of biomaterials leading to implant failure, were found to detect the smallest nanopattern feature size examined in this study (55 nm). Primary macrophages are involved in the inflammatory response to implants and release reactive oxygen species and degradative enzymes. These cells were found to respond only to 200 nm sized nanorods. Endothelial cells, which line blood vessels and mediate vascularization of implant sites, were found to respond to feature sizes greater than 55 nm. Constitutive linear regression models were developed using the present empirical observations to correlate substrate nanotopography with resultant cellular morphology. This quantitative description of the changes in cellular morphology using nondimensional analysis and the Buckingham pi theorem provided an insight into engineering of cell morphology using nanopatterns on Pt-BMG structures. Fibroblasts were further analyzed for changes in focal adhesion formation and intracellular GTPases to explore molecular mechanisms underlying nanopattern-induced cytoskeletal remodeling. Consistent with changes in cell spreading, collagen production was reduced when fibroblasts were grown on nanopatterned BMGs. Finally, focused ion beam scanning electron microscopy (FIB-SEM) was employed to quantify cellular traction forces exerted by the contractile fibroblast cells with nanoscale precision.

RESULTS AND DISCUSSION

Fabrication and Characterization of Nanopatterned BMGs. Platinum-based BMG alloys (Pt-BMGs) offer significant advantages for use as a nanopatterned biomaterial due to demonstrated biocompatibility and an unprecedented combination of elasticity, strength, and ductility.[9] Additionally, Pt-BMGs have a demonstrated high resistance to surface oxidation during thermoplastic forming in air that is ideal for use as a biomaterials.[16] In this work, arrays of nanorods were formed on Pt-based BMG substrates *via* thermoplastic forming of $Pt_{57.5}Cu_{14.7}Ni_{5.3}P_{22.5}$ using alumina templates with nominal pore sizes ranging from 55 to 200 nm, termed "BMG-55", "BMG-100", "BMG-150", and "BMG-200", respectively (Figure 1). In contrast to traditional metal-forming processes that require processing at elevated temperatures to form surface patterns and manipulate microstructures, Pt-BMGs are processed at low temperatures (below 300 °C) in air, similar to thermoplastics (Figure 1A). Moreover, the TPF fabrication process eliminates the need for photolithography or other cleanroom-related processing, thus allowing rapid and cost-effective production of nanopatterned Pt-BMGs with high aspect ratio structures (Figure 1B,C).

Thermoplastic forming of BMGs in air is impacted by several parameters including maximum applied force during forming, duration of the applied force, and viscosity of the BMG (Figure 1C). The viscosity BMGs is dependent not only on the precision of the BMG composition, but also on the crystallization kinetics dictated by the critical cooling rate during quenching as part of the BMG casting process.[17] In order to produce BMG substrates with reproducible aspect ratios and substrate sizes for use in this study, the processing parameters of the TPF process were modified to account for slight batch-to-batch variation in the as-cast Pt-BMG material.

Since in excess of 100 samples were utilized for the present study, extensive quality control measures were used to ensure the fidelity of the nanopatterned substrates. Specifically, SEM characterization of the nanopatterned substrates was completed for each batch of samples to verify consistent nanotopography. In addition, EDX was employed to confirm the integrity of the nanopattern surface, the absence of residuals from the KOH wet etch process, and other contaminants.

Growing evidence suggests that surface topography presents biomechanical cues that are important in regulating cell behavior, which can be adjusted to manipulate cell functions such as protein production, contractility, morphology, migration, focal adhesion formation, and stem cell differentiation.[1−5,18] Nanopatterned Pt-BMGs provide a unique platform to investigate these phenomena *in vitro* because modified surfaces can be fabricated with unprecedented precision. Moreover, substrate stiffness as perceived by cells can be modified without compromising the mechanical properties of the bulk material.[19] Therefore altering the surface topography by engineering nanoscale structures is a means to modify the effective surface

A

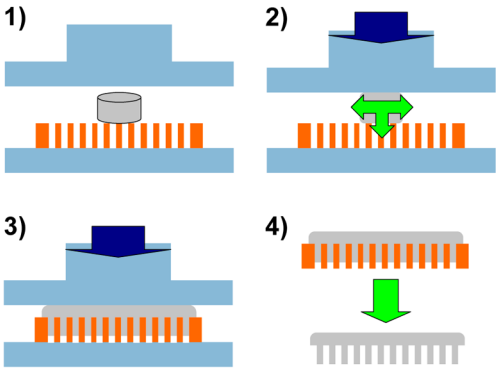

B

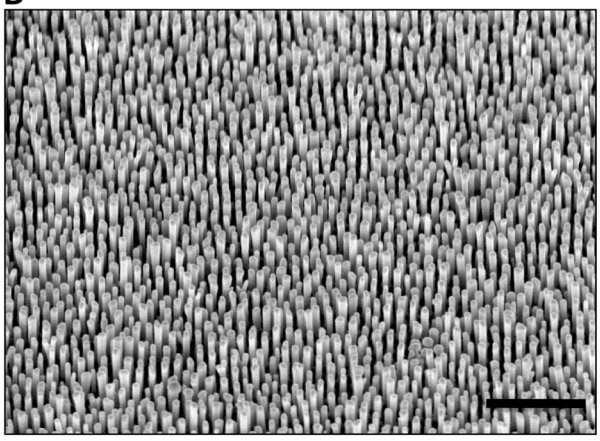

C

BMG Nanopattern Identifier	Nanorod Diameter (nm)	Nanorod Height (nm)	Aspect Ratio (Height : Diameter)	Mold Nanopore Density (Pores/cm^2)	Maximum Applied TPF Force (kN)
BMG-55	64 ± 10	443 ± 121	6.9	6.0x10^9	50
BMG-100	113 ± 14	1103 ± 146	9.8	2.0x10^9	40
BMG-150	181 ± 18	1134 ± 210	6.3	2.0x10^9	30
BMG-200	247 ± 27	1755 ± 214	7.1	1.4x10^9	25

Figure 1. Fabrication and characterization of nanopatterned BMGs. (A) Schematic illustrating cross sectional view of the thermoplastic forming process utilized to fabricate nanopatterned BMG substrates in which the following occur: (1) BMG alloy $Pt_{57.3}Cu_{14.6}Ni_{5.3}P_{22.8}$ was placed on the top exposed surface of a preheated alumina nanoporous mold located between planarized metal plates heated to 540 K. (2) Upon the application of compressive force *via* the planarized plates above the glass transition temperature, T_g, of the BMG alloy, the material began to flow and entered the nanopores on the exposed mold surface. (3) While the BMG remained in an amorphous state above T_g, the applied compressive force was incrementally increased to a maximum threshold ranging from 25 to 50 kN, dependent upon nanorod diameter. The duration of processing time above T_g was approximately 7 min for all nanopatterns in order to prevent crystallization of the BMG. Because of both capillarity and applied force, the nanopatterned area of the BMG substrate continued to increase radially in diameter. (4) The alumina molds were dissolved in potassium hydroxide solution to obtain nanopatterned BMG substrates. (B) Representative SEM image of homogeneous and precise nanorod arrays on a nanopatterned BMG-55 substrate. (C) Summary of the characterized physical properties and processing conditions of thermoplasticaly formed Pt-BMG nanopatterned substrates, including measured nanorod dimensions for nanorod diameter, height, and aspect ratio based on characterization and statistical analysis of in excess of 100 nanopatterned substrates. The nanorod density values are equivalent to the pore density, which is provided by the alumina mold manufacturers. Tolerance values in (C) represent the standard deviation of the population. Scale bar, 1 μm (B).

stiffness to be lower than that of conventional bulk materials.[20] Thus, by modulating the effective surface stiffness, the negative consequences of mechanical compliance mismatch between tissue and implants can be ameliorated.[19,21−23]

Cell Responses to Nanopatterned BMGs. Influence of nanotopography on cellular morphology was assessed by monitoring cytoskeletal remodeling on nanopatterned Pt-BMG substrates. Cell adhesion and survival were supported by all nanopatterned Pt-BMGs (Supporting Information, Figure S1). To monitor changes in cell morphology induced by nanopatterns, cells were seeded onto patterned or flat control BMGs for 24 h. Cells were subsequently fixed, stained, and imaged using fluorescence microscopy. Changes in the morphology of fibroblasts, bone marrow-derived macrophages, and human umbilical vein endothelial cells (HUVECs), all of which are relevant to FBR and tissue regeneration processes, were evaluated by examining actin cytoskeletal remodeling. Distinct changes were observed for all cell types, with the resulting cellular morphologies dependent on nanorod dimensions (Figure 2 and 3). Fibroblasts became increasingly smaller, more circular, and less elongated on the BMGs with increasing nanopattern feature size. This behavior suggests that fibroblast mechanosense and respond to surface topography for all studied nanopatterns. Interestingly, macrophage morphology on the flat BMG control was similar to that on BMG-55, BMG-100, and BMG-150. In contrast, macrophage morphology differed appreciably on BMG-200 nanopattern, indicating that within the range utilized in these studies the smallest feature size to induce morphological changes (*e.g.*, approximately 50% change) in macrophages is 200 nm. HUVECs on flat BMG and BMG-55 were similar in area, but

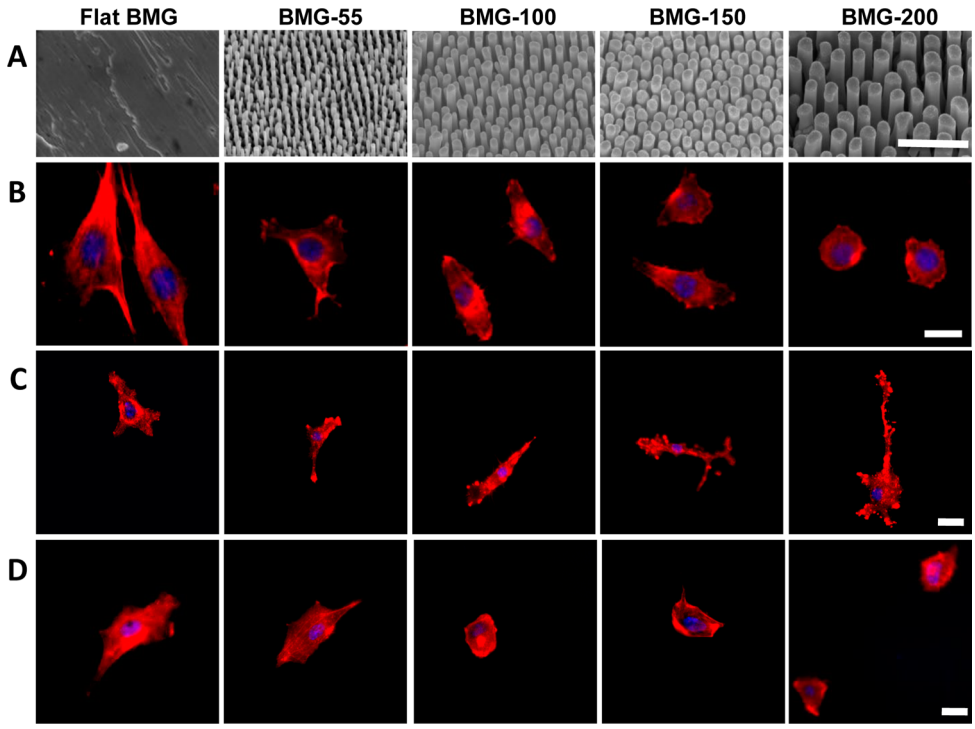

Figure 2. Changes in cellular morphology induced by nanopatterned BMGs. (A) Scanning electron micrographs of representative fabricated flat and nanopatterned BMGs. (B) Representative image of 3T3 fibroblasts, (C) bone marrow derived macrophages, and (D) HUVECs grown on BMGs for 24 h. Cells are stained for F-actin (red) and nucleus (blue). Scale bars, 1 μm (A) and 20 μm (B,C,D).

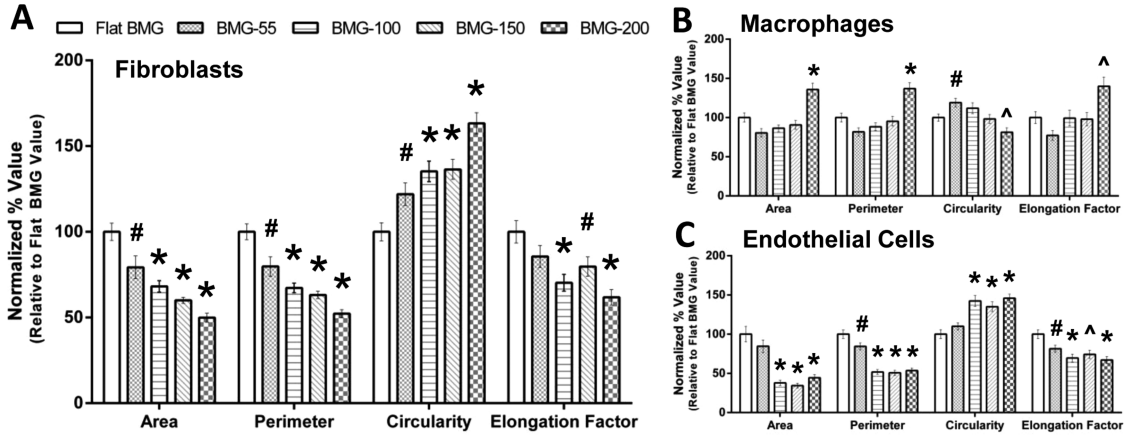

Figure 3. Changes in cellular morphology induced by nanopatterned BMGs. (A) Quantification of changes in 3T3 fibroblast morphology induced by nanopatterned BMGs. (B) Quantification of changes in macrophage morphology induced by nanopatterned BMGs. (C) Quantification of changes in HUVEC morphology induced by nanopatterned BMGs. For (A–C), $n \geq 50$ cells were analyzed for each condition cell morphology quantification. Circularity was defined as [4π(cell area)/(cell perimeter)^2]. Elongation factor was defined as the ratio between the long axis of the cell and the longest axis perpendicular to the long axis ($^{\#}p < 0.05$, $^{\wedge}p < 0.005$, $^{*}p < 0.0005$, *t*-test, comparison to value of corresponding parameter for flat BMG control). Error bars represent the standard error of mean.

had lower area, perimeter, elongation factor, and higher circularity on BMG-100, BMG-150, and BMG-200 substrates. These observations suggest that nanofeatures greater than 55 nm are required to induce morphological changes in HUVECs. Using the criterion of actin cytoskeleton remodeling in fibroblasts, macrophages, and HUVECs, these studies show that nanopattern feature size detection is cell type-dependent.

Cytoskeletal remodeling induced by nanotopography has been described previously. Nanorods have been shown to induce a decrease in fibroblast cell spreading, which is consistent with the findings of the present study.[24−26] Conflicting reports exist on the influence of nanotopography on endothelial cell spreading, but high aspect nanorods (as opposed to low aspect ratio nanorods) have been shown to

decrease cell spreading, similar to our findings.[26,27] Although randomly oriented nanorods have been shown to decrease macrophage cell spreading, there is some evidence to suggest that nanotopography can induce cell spreading in macrophages as well.[28,29] While changes in cellular morphology induced by nanotopography has been described before, the current study provides a systematic examination of well-characterized high aspect ratio nanorods with feature sizes in the range of 55 to 200 nm to identify cell type-specific responses.

Biomaterial acceptance/rejection is mediated primarily by macrophages, and the subsequent fibrotic response by a variety of cell types including fibroblasts and endothelial cells. To design surface nanopatterns that can limit biomaterial rejection and increase implant longevity, it is important to differentially engineer multiple cell types *in vivo*. The present results indicate that some cells such as fibroblasts can detect nanopatterns as small as 55 nm in size, while macrophages do not respond to nanopatterns smaller than 150 nm. Characterization of these cell type-specific responses to feature sizes will be critical in order to hone in on the range of effective nanopatterns relevant for specific *in vivo* applications. The ability to induce specific responses will also be important in the design of nanopatterns that engineer one cell type and not affect other cell types in the microenvironment. Such work will also help identify relevant length scales for further investigation of the role of nanotopographical cues inherent in healthy and diseased tissue, and associated extracellular matrix. Along with examining the effect of nanotopography on cell function, consolidative efforts toward characterizing cell type-specific detection limits will be key to understanding and exploiting cell–nanotopography interactions for biomedical applications.

Quantitative Correlations between Cell Morphology and BMG Nanotopography. Using nondimensional analysis based on the Buckingham pi theorem, changes in cell morphology and substrate nanotopography were quantitatively correlated (Supporting Information II). Multiple linear regression was employed to describe the correlation among three nondimensional variables: percent change in cell circularity induced by nanopatterns (S), nanorod dimension parameter (N), and nanorod surface area parameter (SA_N). Fibroblast circularity correlated to BMG nanotopography as follows:

$$S = -9485.79\,(N) + 2.96\,(SA_N) + 0.25 \qquad (1)$$

Analysis can be extended to correlate substrate nanotopography to cellular protein expression and genetic profiles, ultimately leading to informed design of nanopatterned biomaterials to induce anti-inflammatory and regenerative cellular phenotypes.

Biomechanical Cues Underlying Cell–Nanopattern Interactions Govern Cell Activity. The complex interactions between cells and nanorods required a multifaceted approach to investigate the potential mechanisms dictating the cytoskeletal remodeling observed by fluorescence imaging. Biochemical assays were performed to investigate the molecular basis for changes in cell morphology. Additionally, novel electron microscopy techniques were employed to image cell–nanorod interactions and quantify cellular traction forces with nanoscale precision. Fibroblasts were selected for these additional analyses since they exhibited changes in morphology when exposed to the entire range of nanopatterned BMG substrates. Additionally, fibroblasts are critical to the foreign body response as primary contributors of the fibrotic encapsulation that often renders implantable materials nonfunctional.

In order to investigate the molecular mechanisms underlying fibroblast–nanopattern interactions, nanopattern-induced changes in adsorption of the serum proteins, formation of focal adhesions, expression of downstream effector Rho-A GTPase, and collagen production were analyzed. Changes in BMG nanopattern dimensions consequentially modulated the extent and distribution of fibronectin absorption from serum-containing culture media (Supporting Information, Figure S2). Modifications of focal adhesion formation in fibroblasts in response to nanopatterns were analyzed by immunofluorescent detection of paxillin. Focal adhesion density increased with increasing nanopattern feature size, corresponding to the reduced size of fibroblasts on nanopatterned BMGs (Figure 4A,C). In addition, intracellular levels of active Rho-A, a small GTPase that regulates actin remodeling, were significantly lower in fibroblasts grown on BMG-55s and BMG-200s in comparison to flat BMG control (Figure 4D).

Furthermore, fibroblasts grown on nanopatterned substrates were observed to produce significantly less collagen-I than fibroblasts grown on flat BMGs (Figure 4B,E). Nanopattern-induced reduction in spreading of fibroblasts corresponded to a change in the fibrotic phenotype of these cells. Collagen-I production by fibroblasts leads to fibrosis in diseased tissue as well as encapsulation of biomaterials *in vivo,* leading to implant failure. These results indicate that nanopatterning of BMGs can influence cell function by significantly inhibiting matrix production by fibroblasts.

Taken together, these results suggest that biomechanical cues mediate cellular sensing of substrate nanotopography, which therefore influences cell function. Varying the nanopattern dimensions alters the adsorption patterns of serum protein and effective substrate stiffness, leading to changes in cellular focal adhesion formation. Changes in focal adhesion density, which correspond to effective nanorod stiffness, lead to changes in intracellular cytoskeletal remodeling proteins. Specifically, increasing focal adhesion density corresponds with decreasing active Rho-A GTPase levels, resulting in reduced cell spreading and

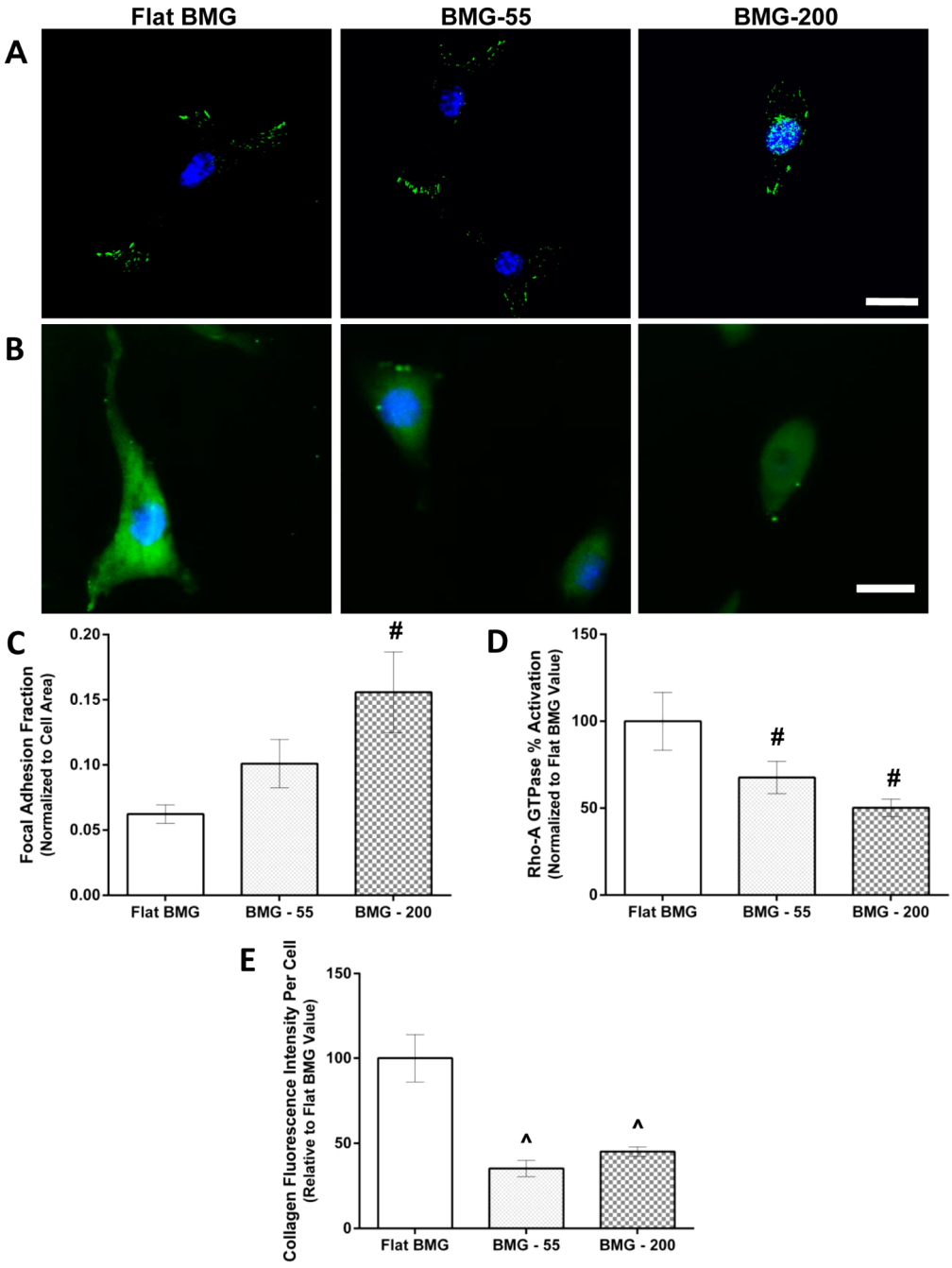

Figure 4. Molecular mechanisms underlying fibroblast−nanopattern interactions. (A) Representative images of fluorescently labeled paxillin (green) and cell nuclei using DAPI (blue) in 3T3 fibroblast cells grown for 24 h on BMGs. (B) Representative images of 3T3 fibroblasts fluorescently labeled for collagen I (green) and DAPI (blue). (C) Cells were analyzed for each condition to quantify the focal adhesion fraction and (D) Rho-A activation. (E) Quantification of collagen production in fibroblasts grown on BMGs using the integrated fluorescence intensity ($^{\#}p < 0.05$, $^{\wedge}p < 0.005$, *t*-test, comparison to value of corresponding parameter for flat BMG control). Error bars represent the standard error of mean. Scale bar, 20 μm (A,B).

decreased collagen production. By modifying cell function through altering the fibrotic response, nanopatterned BMGs may provide a viable approach to control biomaterial rejection and increase implant lifetime.

Cellular Traction Force Measurement. To gain additional insight into the mechanical mechanisms underlying the cell−nanorod interactions, scanning electron microscopy (SEM) was employed. Analysis of cells with this method corroborated the trends in cell spreading observed using fluorescence microscopy. In addition, extensive bending of the nanorods at the cell perimeter was revealed, as reported previously with other patterned substrates (Supporting Information, Figure S3).[5,6,30,31] To examine nanorod bending not visible underneath the cell surface, focused ion beam (FIB) milling was employed to cross-section fibroblasts on nanorods *in situ* (Figure 5A−F). FIB cross-sections revealed no penetration by fibroblast cells into the internanorod space, suggesting that the cells

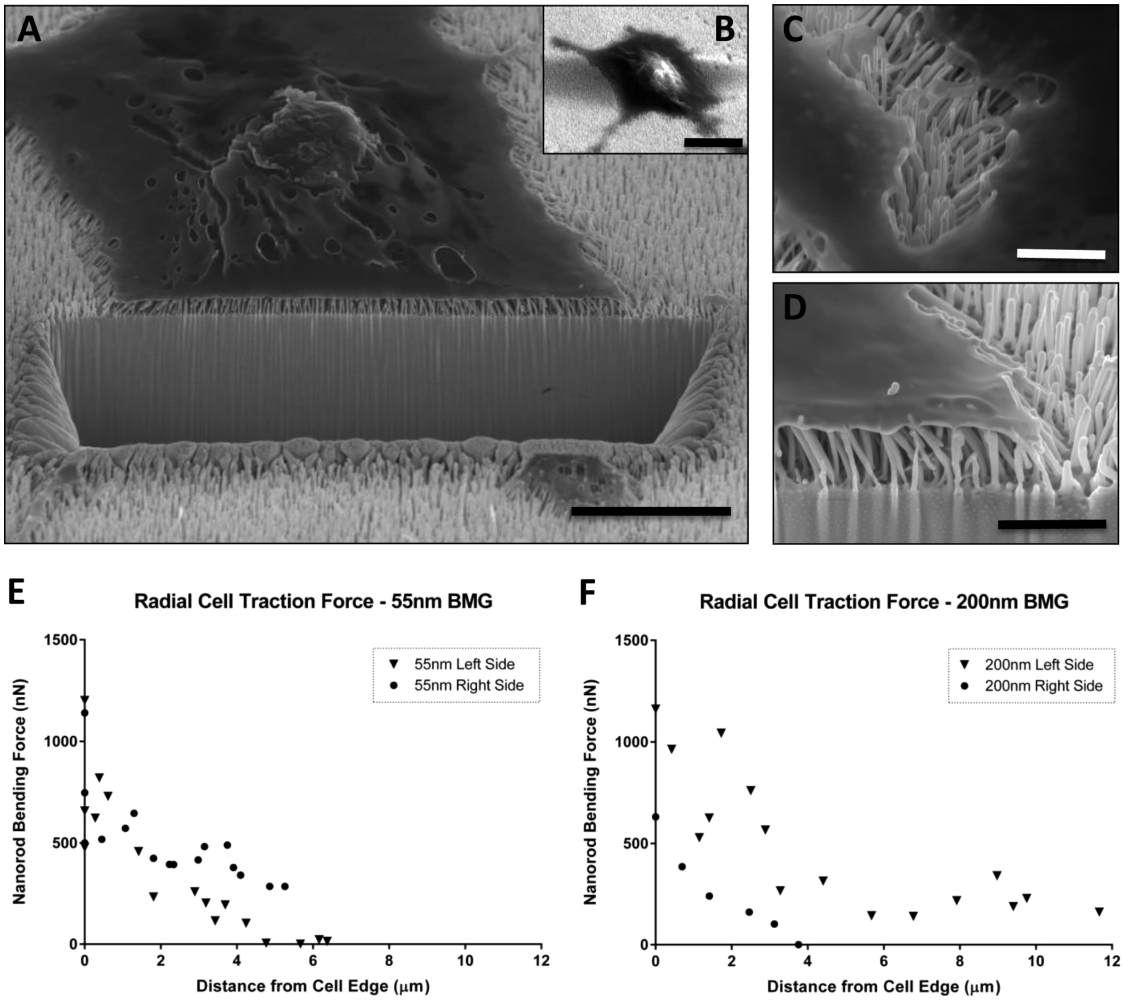

Figure 5. Mechanical mechanisms underlying fibroblast−nanopattern interactions. (A) SEM image of post-FIB cross-sectional cut of a representative fibroblast cell residing on a BMG-55 substrate, which revealed nanoscale rod bending as well as lack of cytoskeletal penetration into the space between the nanorods. (B) SEM image the same fibroblast cell on a BMG-55 substrate depicted in (A) prior to the FIB cross-sectional cut, which illustrates the limitations of traditional electron microscopy due to the lack of visibility of cell−nanorod interaction in areas of the nanopatterned BMG sample on which the cell resides. (C) Representative SEM image of an area of the same fibroblast cell depicted in (A,B) in which a portion of the previously continuous cell was thinned and removed by the FIB process to reveal elastic recovery of nanorod bending demonstrated by erect, unbent rods after layer-by-layer removal of the cell using ion milling, therefore indicating elastic deformation of the nanorods by the cell. (D) High resolution SEM image of the right side of the FIB cut/cell interface depicted in (A). (E) On the basis of the measured nanorod bending angles, the nanorod deflection and corresponding bending force were quantified, and the radial variation of the traction force *versus* distance from the edge of the fibroblast cell along the exposed cross-sectional FIB cut was plotted with nanoscale precision for a BMG-55 substrate. (F) The radial variation of the traction force *versus* distance from the edge of the fibroblast cell along the exposed cross-sectional FIB cut was also plotted with nanoscale precision for a BMG-200 substrate. Scale bars, 5 μm (A); 10 μm (B); 1 μm (C); 1 μm (D).

were sensing and responding to the nanotopography rather than the bulk BMG substrate.

Cell spreading and migration occur in a dynamic environment; therefore, elastic bending of the nanorods is important to ensure that cells perceive consistent nanotopography throughout the lifetime of an implant or device. On the basis of analysis of fibroblasts on BMGs, the resulting maximum stress of approximately 400 MPa exerted on the nanorods was less than the 1400 MPa yield strength of the Pt-BMG alloy.[32] Elastic bending was corroborated further by recovery of erect nanorods following cell removal using surface ion milling (Figure 5C).

Nanorod deflection was observed to increase radially extending outward from the cell, and analysis of the nanorod deflections allowed cellular traction forces to be quantified with nanoscale precision. Local force exerted on the nanorods was determined using the measured individual rod deflections and nominal bending stiffness (Supporting Information I). On the basis of local force calculations, individual traction forces were compiled to form traction force maps with nanoscale resolution for fibroblasts on both BMG-55 and BMG-200 substrates (Figure 5E,F). The maximum calculated deflection of the nanorods was observed to be approximately equivalent for both the BMG-55 and

BMG-200 substrates. Despite differences in the height of the nanorods between the respective substrates, the stiffness of the individual nanorods composing the substrates is approximately equivalent since the aspect ratios of the BMG-200 and BMG-55 substrates were designed to be constant (Figure 1C, Supporting Information I). Therefore, since fibroblasts perceive the same nanorod stiffness, the forces exerted by the cell on the nanorods at the cell perimeter produce a comparable magnitude of deflection for both the BMG-200 and BMG-55 nanopatterns.

While several studies of cell traction forces on microscale structures have proven useful to quantify intracellular forces, such methodologies cannot be extended to the nanoscale because of challenges with resolution.[6,30,33,34] Therefore, the FIB traction force mapping technique provides unprecedented insight into cell–nanopattern interactions in terms of both topography and scale. Conceivably, this methodology may be extended to build more complex traction force maps by integrating data from multiple FIB cross-sections of the same cell. A wide range of values for cellular traction forces, ranging from 1–100 nN for polymeric substrates to 4.7 μN for silicon, have been reported in the literature.[6,30,33–35] Traction force is a function of nanorod stiffness that scales linearly with the elastic modulus of the substrate material (Supporting Information I). Therefore the variation in reported traction force correlates with the elastic modulus of the substrate material, which can range in magnitude from 2 MPa for polymers such as PDMS to 151 GPa for silicon. Since $Pt_{57.5}Cu_{14.7}Ni_{5.3}P_{22.5}$ has an elastic modulus of 94.8 GPa,[32] the maximum observed cellular traction force value of 1.2 μN (Figure 5E,F) is consistent with the previously reported values. These trends illustrate the dynamic reciprocity between traction forces imparted by the cell and the inherent material properties of the substrate and associated nanotopography.

CONCLUSION

In summary, this study highlights how nanopatterned BMGs comprise a versatile class of materials for load bearing or structural implants that incorporate tunable surface features to drive cell-specific behaviors without the use of exogenous growth factors. Specifically, the detection of nanopatterns varied markedly according to cell type, ranging from as high as 200 to 55 nm or lower. Additional characterization of the sensitivity of cells to nanopatterns will be crucial for designing biomaterials that could selectively influence multiple cell types *in vivo*. In addition, novel FIB microscopy techniques enabled traction force measurements and the examination of cell–nanorod interactions with nanoscale precision. Coupled with nondimensional statistical analysis, these results provide new insights to stiffness-induced cell behaviors, the limits of biomechanical detection in a variety of cells, and a foundation for rational design of nanopatterned materials to attenuate biomaterial rejection. This approach can be extended to analyze the response of other relevant cell types associated with tissue regeneration and FBR, including mesenchymal stem cells. Thus, nanopatterned BMGs can be used to design cell-instructive constructs that retain bulk material integrity for use in biomedical applications.

METHODS

Fabrication of Nanopatterned BMG Substrates. Platinum-based BMG alloy used to form the nanopatterned BMG substrates was cast from constituent high-purity raw materials, including platinum, phosphorus, nickel, and copper, as described in detail previously.[15,32] The Pt-BMG bulk alloy was cut into cylindrical samples approximately 2 mm in diameter and a height of 2 mm using a diamond saw, and the cylindrical samples were ultrasonically cleaned using acetone and isopropanol. Fabrication of the nanopatterned BMGs *via* isothermal molding was carried out in air at a processing temperature of 540 K using a compression tester (Instron Model 5569), with variable applied loads with maximum loads ranging from 25 to 50 kN depending on the nanopattern feature size, as given in Figure 1C. Commercially available nanoporous alumina (Al_2O_3) membranes with nominal pore sizes of 55, 100, 150 (Synkera), and 200 nm (Whatman) were used as templates for the TPF process. The nanopatterned BMGs were soaked in a solution of 30% KOH for 2 h to dissolve the alumina molds; after mold removal, the nanopatterned BMGs were subjected to a cleaning regimen consisting of acetone followed by isopropanol.

Serum Fibronectin Deposition on Nanopatterned BMGs. Nanopatterned BMG substrates were sterilized with 70% ethanol for 1 h and washed with phosphate buffered saline (PBS). Subsequently, BMGs were incubated in Dulbecco's modified Eagle's medium (DMEM) (GIBCO), supplemented with 10% fetal bovine serum (FBS) for 3 h. Media were aspirated, and BMGs were fixed with 4% paraformaldehyde (JT Baker). BMGs were then washed with PBS, blocked with 1% Bovine serum albumin (BSA) (Sigma-Aldrich) for 45 min, and washed again. BMGs were then incubated with rabbit anti-fibronectin (AbCam) for 1 h at room temperature followed by a FITC-conjugated secondary antibody (AbCam) for 30 min at room temperature. Then the BMGs were washed with PBS and mounted on a glass slide with mounting medium (Vectashield) and viewed under a fluorescence microscope (Zeiss). Images were analyzed for percentage area staining positive for fibronectin using image analysis software (Metamorph).

Cell Culture. NIH 3T3 fibroblasts were maintained in DMEM supplemented with 10% FBS and 1% penicillin–streptomycin–glutamate. Human umbilical cord vein cells (HUVECs) were maintained in M199 medium (Gibco) supplemented with 20% FBS and 1% penicillin–streptomycin–glutamate. Bone marrow-derived macrophages were generated by expansion of bone marrow cells from 3–6 month old mice as described previously.[36]

Cell Viability Assay. To evaluate cell viability on the BMG substrates, 7500 cells/cm^2 were seeded on each disk and cultured with appropriate media for 24 h. Cell seeded BMGs were triple stained with calcein (Molecular Probes) for live cell cytoplasm, ethidium homodimer (Molecular Probes) for dead cell nuclei, and Hoescht dye (Molecular Probes) to stain all cell nuclei. BMGs were then imaged with fluorescence microscopy, and the ratio of live cells to total number of cells per field of view was reported as the percentage of live cells was estimated for each type of BMGs.

Immunofluorescence Staining of Cells. Cells were seeded and cultured on disks for 24 h with appropriate media. Media was then aspirated, and cells were fixed with 4% paraformaldehyde. Cells were permeabilized with 0.1% Triton X-100 for 10 min, washed and stained with DAPI (blue nuclear stain) and Rhodamine-phallodin (red stain for F-actin) for 30 min at room temperature. BMG Disks were subsequently washed and mounted on a glass slide for imaging with a fluorescence microscope (Zeiss).

Quantification of Cellular Morphology. Individual cells were analyzed with NIH image analysis software Image J. Four different morphologic parameters: area, perimeter, circularity, and elongation factor, were measured and averaged for at least 50 cells for each type of nanopatterned BMG substrate. Circularity was defined as $[4\pi(\text{cell area})/(\text{cell perimeter})^2]$. Elongation factor was calculated as the length of the long axis of the cell divided by the lengthiest axis perpendicular to the long axis as described by Lamers *et al.*[18] These morphologic parameters were expressed as percentage of the respective parameter value for the control condition as described by Wittmer *et al.*[37] Flat BMGs were used as the control to analyze the effect of substrate nanopatterns on cell morphology.

SEM and FIB Analysis of Cell–BMG Interaction. Cells were seeded and cultured on BMG substrates for 24 h with appropriate media. Media was aspirated, and BMGs were soaked in PBS. PBS was aspirated, and BMGs were incubated in 1% glutaraldehyde in 0.1 M Cacodylate buffer for 5 min. BMGs were then washed with distilled water for 5 min. BMGs were dehydrated using a series of ethanol washes with increasing concentration from 70% to 100% ethanol for 5 min each. BMGs were subsequently immersed in hexamethyldisilazane for 15 min. Prior to imaging, the BMGs were air-dried and then sputter coated with a layer of Cr with a thickness of approximately 5 nm. Imaging was completed using an SEM (Hitachi SU-70). The same samples used for SEM analysis were used to obtain FIB cross sections. A dual-beam FIB (FEI NanoLab 600 Dual Beam FIB) was employed to mill cross sections of cells residing on nanorods and obtain SEM images of the FIB cross section for analysis. Using image analysis software (Quartz PCI), nanorod bending observed in the FIB cross section images was measured as the bending angle of the in-plane nanorods that were visibly connected to both the cell and substrate (Supporting Data I).

Rho-A GTPase Assay. Cells were seeded and cultured on BMG substrates for 1 h, 15 min with appropriate media. Cell lysates were obtained, and the intracellular active Rho-A GTPase was estimated using a GLISA Rho-A assay kit (Cytoskeleton).

Focal Adhesion Staining. Cells were seeded and cultured on BMG substrates for 24 h with appropriate media. Media was aspirated, and BMGs were washed with PBS. Cells were permeabilized with 0.1% Triton X-100 for 10 min and blocked with 2% BSA. Cells were washed with PBS and incubated with anti-paxillin primary antibody (Sigma-Aldrich) overnight. BMGs were subsequently washed and stained with a GFP-tagged secondary antibody against paxillin (Life Technologies) and DAPI. BMGs were mounted on a glass slide for fluorescence imaging.

Collagen-I Staining. Cells were seeded and cultured on BMG substrates for 24 h with appropriate media. Media was aspirated, and BMGs were washed with PBS. Cells were permeabilized with 0.2% Triton X-100 for 10 min. Cells were washed with PBS and incubated with collagen type I primary antibody (Abcam) for an hour at room temperature. BMGs were subsequently washed and stained with a secondary Alexa 488-conjugated antibody and DAPI. BMGs were mounted on a glass slide for fluorescence imaging.

Conflict of Interest: The authors declare no competing financial interest.

Acknowledgment. Facilities used for this work were supported by Yale Institute for Nanoscience and Quantum Engineering and CRISP. A. Sawyer was supported by NIH Vascular Research Training Grant (5T32HL007950-12, A.S.). Additional thanks are offered to the IBM Semiconductor Research and Development Center in Fishkill, New York, for access to the FIB resource. The authors would also like to thank M. Kanik and P. Bordeenithikasem for contributions of time and effort related to the Pt-BMG alloy casting process, L.B. Moore and T. Bancroft for assistance with cell isolations, and J. Humphrey for helpful discussions and critical reading of the manuscript. This work was primarily funded by CRISP (NSF MRSEC DMR 1119826) and National Institutes of Health Grant (GM-072194).

Supporting Information Available: Supporting Information I outlines the quantification of cellular traction forces using FIB-SEM (Part I) and the calculation the effective stiffness of BMG substrates (Part II). Supporting Information II describes the nondimensional analysis and Buckingham pi theorem to correlate substrate nanotopography to cell morphology for all cell types. Figure S1 shows cell viability on BMG substrates. Figure S2 illustrates nanopattern-induced changes in serum protein adsorption on BMG substrates. Figure S3 displays scanning electron micrographs of fibroblasts on nanopatterned BMGs. This material is available free of charge *via* the Internet at http://pubs.acs.org.

REFERENCES AND NOTES

1. Yim, E. K.; Reano, R. M.; Pang, S. W.; Yee, A. F.; Chen, C. S.; Leong, K. W. Nanopattern-Induced Changes in Morphology and Motility of Smooth Muscle Cells. *Biomaterials* **2005**, *26*, 5405–5413.
2. Yim, E.; Darling, E.; Kulangara, K.; Guilak, F.; Leong, K. Nanotopography-Induced Changes in Focal Adhesions, Cytoskeletal Organization, and Mechanical Properties of Human Mesenchymal Stem Cells. *Biomaterials* **2010**, *31*, 1299–1306.
3. McMurray, R. J.; Gadegaard, N.; Tsimbouri, P. M.; Burgess, K. V.; McNamara, L. E.; Tare, R.; Murawski, K.; Kingham, E.; Oreffo, R. O.; Dalby, M. J. Nanoscale Surfaces for the Long-Term Maintenance of Mesenchymal Stem Cell Phenotype and Multipotency. *Nat. Mater.* **2011**, *10*, 637–644.
4. Csaderova, L.; Martines, E.; Seunarine, K.; Gadegaard, N.; Wilkinson, C.; Riehle, M. A Biodegradable and Biocompatible Regular Nanopattern for Large-Scale Selective Cell Growth. *Small* **2010**, *6*, 2755–2761.
5. Bucaro, M. A.; Vasquez, Y.; Hatton, B. D.; Aizenberg, J. Fine-Tuning the Degree of Stem Cell Polarization and Alignment on Ordered Arrays of High-Aspect-Ratio Nanopillars. *ACS Nano* **2012**, *6*, 6222–6230.
6. Chang, J. K.; Li, C. J.; Liao, H. J.; Wang, C. K.; Wang, G. J.; Ho, M. L. Anti-Inflammatory Drugs Suppress Proliferation and Induce Apoptosis Through Altering Expressions of Cell Cycle Regulators and Pro-Apoptotic Factors in Cultured Human Osteoblasts. *Toxicology* **2009**, *258*, 148–156.
7. Lu, J.; Rao, M. P.; MacDonald, N. C.; Khang, D.; Webster, T. J. Improved Endothelial Cell Adhesion and Proliferation on Patterned Titanium Surfaces with Rationally Designed, Micrometer to Nanometer Features. *Acta Biomater.* **2008**, *4*, 192–201.
8. Variola, F.; Brunski, J. B.; Orsini, G.; Tambasco de Oliveira, P.; Wazen, R.; Nanci, A. Nanoscale Surface Modifications of Medically Relevant Metals: State-of-the-Art and Perspectives. *Nanoscale* **2011**, *3*, 335–353.
9. Schroers, J.; Kumar, G.; Hodges, T.; Chan, S.; Kyriakides, T. Bulk Metallic Glasses for Biomedical Applications. *JOM* **2009**, *61*, 21–29.
10. Zberg, B.; Uggowitzer, P. J.; Loffler, J. F. MgZnCa Glasses without Clinically Observable Hydrogen Evolution for Biodegradable Implants. *Nat. Mater.* **2009**, *8*, 887–891.
11. Magagnosc, D. J.; Ehrbar, R.; Kumar, G.; He, M. R.; Schroers, J.; Gianola, D. S. Tunable Tensile Ductility in Metallic Glasses. *Sci. Rep.* **2013**, *3* (1096), 1–6.
12. Tian, L.; Cheng, Y. Q.; Shan, Z. W.; Li, J.; Wang, C. C.; Han, X. D.; Sun, J.; Ma, E. Approaching the Ideal Elastic Limit of Metallic Glasses. *Nat. Commun.* **2012**, *3* (609), 1–6.
13. Volkert, C. A.; Donohue, A.; Spaepen, F. Effect of Sample Size on Deformation in Amorphous Metals. *J. Appl. Phys.* **2008**, *103* (083539), 1–6.
14. Jang, D. C.; Greer, J. R. Transition from a Strong-Yet-Brittle to a Stronger-and-Ductile State by Size Reduction of Metallic Glasses. *Nat. Mater.* **2010**, *9*, 215–219.

15. Kumar, G.; Tang, H. X.; Schroers, J. Nanomoulding with Amorphous Metals. *Nature* **2009**, *457*, 868–872.
16. Schroers, J. On the Formability of Bulk Metallic Glass in Its Supercooled Liquid State. *Acta Mater.* **2008**, *56*, 471–478.
17. Pitt, E. B.; Kumar, G.; Schroers, J. Temperature Dependence of the Thermoplastic Formability in Bulk Metallic Glasses. *J. Appl. Phys.* **2011**, *110* (043518), 1–7.
18. Lamers, E.; van Horssen, R.; te Riet, J.; van Delft, F. C.; Luttge, R.; Walboomers, X. F.; Jansen, J. A. The Influence of Nanoscale Topographical Cues on Initial Osteoblast Morphology and Migration. *Eur. Cells Mater.* **2010**, *20*, 329–343.
19. Stevens, M. M.; George, J. H. Exploring and Engineering the Cell Surface Interface. *Science* **2005**, *310*, 1135–1138.
20. Silva, E. C.; Tong, L.; Yip, S.; Van Vliet, K. J. Size Effects on the Stiffness of Silica Nanowires. *Small* **2006**, *2*, 239–243.
21. Discher, D. E.; Janmey, P.; Wang, Y. L. Tissue Cells Feel and Respond to the Stiffness of Their Substrate. *Science* **2005**, *310*, 1139–1143.
22. Williams, D. F. On the Mechanisms of Biocompatibility. *Biomaterials* **2008**, *29*, 2941–2953.
23. Hilborn, J.; Bjursten, L. M. A New and Evolving Paradigm for Biocompatibility. *J. Tissue Eng. Regener. Med.* **2007**, *1*, 110–119.
24. Kam, K. R.; Walsh, L. A.; Bock, S. M.; Ollerenshaw, J. D.; Ross, R. F.; Desai, T. A. The Effect of Nanotopography on Modulating Protein Adsorption and the Fibrotic Response. *Tissue Eng., Part A* **2014**, *20*, 130–138.
25. Dalby, M. J.; Riehle, M. O.; Sutherland, D. S.; Agheli, H.; Curtis, A. S. Morphological and Microarray Analysis of Human Fibroblasts Cultured on Nanocolumns Produced by Colloidal Lithography. *Eur. Cells Mater.* **2005**, *9*, 1–8.
26. Lee, J.; Kang, B. S.; Hicks, B.; Chancellor, T. F., Jr.; Chu, B. H.; Wang, H. T.; Keselowsky, B. G.; Ren, F.; Lele, T. P. The Control of Cell Adhesion and Viability by Zinc Oxide Nanorods. *Biomaterials* **2008**, *29*, 3743–3749.
27. Dalby, M. J.; Riehle, M. O.; Johnstone, H.; Affrossman, S.; Curtis, A. S. *In Vitro* Reaction of Endothelial Cells to Polymer Demixed Nanotopography. *Biomaterials* **2002**, *23*, 2945–2954.
28. Chen, S.; Jones, J. A.; Xu, Y.; Low, H. Y.; Anderson, J. M.; Leong, K. W. Characterization of Topographical Effects on Macrophage Behavior in a Foreign Body Response Model. *Biomaterials* **2010**, *31*, 3479–3491.
29. Zaveri, T. D.; Dolgova, N. V.; Chu, B. H.; Lee, J.; Wong, J.; Lele, T. P.; Ren, F.; Keselowsky, B. G. Contributions of Surface Topography and Cytotoxicity to the Macrophage Response to Zinc Oxide Nanorods. *Biomaterials* **2010**, *31*, 2999–3007.
30. Tan, J. L.; Tien, J.; Pirone, D. M.; Gray, D. S.; Bhadriraju, K.; Chen, C. S. Cells Lying on a Bed of Microneedles: An Approach to Isolate Mechanical Force. *Proc. Natl. Acad. Sci. U. S. A.* **2003**, *100*, 1484–1489.
31. Pokroy, B.; Epstein, A. K.; Persson-Gulda, M. C. M.; Aizenberg, J. Fabrication of Bioinspired Actuated Nanostructures with Arbitrary Geometry and Stiffness. *Adv. Mater.* **2009**, *21*, 463–469.
32. Schroers, J.; Johnson, W. L. Ductile Bulk Metallic Glass. *Phys. Rev. Lett.* **2004**, *93* (255506), 1–4.
33. du Roure, O.; Saez, A.; Buguin, A.; Austin, R. H.; Chavrier, P.; Silberzan, P.; Ladoux, B. Force Mapping in Epithelial Cell Migration. *Proc. Natl. Acad. Sci. U. S. A.* **2005**, *102*, 2390–2395.
34. Lemmon, C. A.; Romer, L. H. A Predictive Model of Cell Traction Forces Based on Cell Geometry. *Biophys. J.* **2010**, *99*, L78–L80.
35. Saez, A.; Anon, E.; Ghibaudo, M.; du Roure, O.; Di Meglio, J. M.; Hersen, P.; Silberzan, P.; Buguin, A.; Ladoux, B. Traction Forces Exerted by Epithelial Cell Sheets. *J. Phys.: Condens. Matter* **2010**, *22* (194119), 1–9.
36. Jay, S. M.; Skokos, E.; Laiwalla, F.; Krady, M. M.; Kyriakides, T. R. Foreign Body Giant Cell Formation is Preceded by Lamellipodia Formation and Can be Attenuated by Inhibition of Rac1 Activation. *Am. J. Pathol.* **2007**, *171*, 632–640.
37. Wittmer, C. R.; Phelps, J. A.; Saltzman, W. M.; Van Tassel, P. R. Fibronectin Terminated Multilayer Films: Protein Adsorption and Cell Attachment Studies. *Biomaterials* **2007**, *28*, 851–860.